Chapter 3

The effects of 2D materials on semiconductor/liquid junctions

Covalent functionalization of semiconductor surfaces is a well-explored method for shifting band edge positions. However, the process of discovering the chemistry needed for such functionalization can be time-consuming and this strategy is not easily translated between materials without extensive work to develop new reactions. Recently, covering n-type silicon with single layer graphene and its derivative, fluorinated graphene, was reported as a portable strategy for protection against oxidation during photoanodic operation in aqueous solution. In addition, the open-circuit potential of these electrodes was shown to shift in contact with a series of nonaqueous redox couples of varying potentials, indicating a lack of Fermi-level pinning despite the Dirac point of graphene lying mid-gap to silicon (-4.55 eV vs. vacuum).

Further understanding the effect of the density of states of a 2D material on an interface is key to the successful integration of these materials into devices. Many of the extraordinary properties that have made graphene so well studied arise from the existence of a Dirac point in the density of states, which also introduces a finite number of surface states within the band gap of silicon. These states contribute to the formation of a rectifying potential-dependent barrier height in contact with both n-type and p-type silicon unlike the potential-independent barrier heights of semiconductor-electrolyte and semiconductor-metal interfaces. However, these states, and resulting dependence of barrier height on potential, can also attenuate the barrier height of fabricated devices by partially pinning the interface. In contrast, hexagonal boron nitride (h-BN), an analogue of graphene consisting of an alternating lattice of boron and nitrogen atoms, is primarily used as an inert protective layer on 2D material heterostructures. h-BN is known to be a good insulator with a bandgap of 5.97 eV. The lack of states within the bandgap of silicon make it an excellent endpoint for comparison with graphene, as the bandgaps of most 2D materials fall between the range presented by these two materials (0 eV-5.97 eV) and the behavior of each at an interface should be significantly different given their widely varying properties.

Here we probe the effect of 2D materials with significantly different distributions of density of state by comparing the impact of graphene (Gr) and hexagonal boron nitride (h-BN) on the photoelectrochemical performance of p-type silicon. Inserting two-dimensional (2D) materials at the semiconductor/liquid junction should have an impact on junction energetics through the equilibration of the Fermi levels of the semiconductor and the 2D material, depending on the density of states of the interstitial 2D material.

Although single crystals of 2D materials can be obtained through mechanical exfoliation of layered materials, these methods do not produce single crystals of a size large enough to cover even lab scale (~1 cm^2) photoelectrodes. Due to the large area needed, chemical vapor deposition grown (CVD) 2D materials are used because large (>1 cm^2) area samples can easily be produced. However, CVD grown graphene and h-BN are both polycrystalline materials that inherently contain grain boundaries and defects. There is a distinct difference between the electronic structure of the pristine material and the defective sites, which [are known to] locally impact the energetics at the semiconductor/liquid junction. Both the magnitude of such local differences and their influence on macroscale behavior remain as open questions. To address this issue, scanning electrochemical cell microscopy (SECCM) is demonstrated here as a tool to study junction energetics with submicron spatial resolution.

SECCM is a scanning probe microscopy technique that utilizes an electrolyte-filled glass nanopipette as the probe. The counter and reference electrodes of an electrochemical cell are housed within this pipette and connected to a potentiostat. Using a micropositioner, the opening of the pipette is brought close to a surface operating as the working electrode until a nanoscale liquid junction is formed between the pipette and the surface, completing the circuit for the electrochemical cell. The probe is then operated as an electrochemical cell with a working electrode area defined by the size of the liquid junction. SECCM allows standard electrochemical techniques to be performed with a high degree of spatial resolution, and has previously been used in PEC systems to measure resolve photocurrents on heterogeneous surfaces. Beyond enabling spatially resolved electrochemistry, the small surface area of the working electrode in contact with electrolyte makes SECCM ideal for samples that readily degrade or change structure under electrochemical operation, as a location can be tested without affecting the remainder of the sample. Demonstrating the utility of SECCM as a general technique for evaluation of PEC behavior on silicon, a readily available, stable, and well-characterized material, will set the stage for studying materials where the features of SECCM are necessary.

Here we compare the photoelectrochemical behavior of graphene and h-BN covered p-Si photoelectrodes to H-terminated Si (111) surfaces using both macro- and nano-scale photoelectrochemical measurements. We show that h-BN covered electrodes do not exhibit strong evidence of Fermi level pinning while the graphene exhibits evidence of partial Fermi level pinning. Both graphene and h-BN shift the flat band potential of the p-Si to negative potentials relative to the bare surface, resulting in lower open circuit voltages (V_{OC}) for these photoelectrodes in contact with a series of redox couples in solution. Additionally, we show that nanoscale SECCM measurements of V_{OC} correlate well to macroscale observations and replicate observed trends. Finally, we establish the ability of SECCM to elucidate local variability of V_{OC} to demonstrate its future applicability as a technique for imaging semiconductor/liquid junction energetics with nanoscale resolution.

Methods

Materials

Acetonitrile (Dri-Solv, 99.9%) was purchased from Fisher Scientific and used as received. Lithium perchlorate ($LiClO_4$, 99.99%, battery grade) was purchased from Sigma Aldrich and used as received.

Ferrocene (Fc), dimethylferrocene (DiMeFc), nickelocene (Nc), decamethylferrocene (DeMeFc), and cobaltocene (Cc) were all purchased from Sigma-Aldrich and and purified by sublimation prior to use. Cobaltocenium hexafluorophosphate (Sigma-Aldrich, 98%) was recrystallized from ethanol prior to use.

Methyl viologen hexafluorophosphate ($MV(PF_6)_2$) was prepared by metathesis of methyl viologen dichloride (Sigma-Aldrich, 98%) with ammonium hexfluorophosphate (Sigma-Aldrich, 99.98%) in water and recrystallized from ethanol prior to use.

Following purification or purchase, all chemicals were stored in a N_2-filled flush box for storage. Electrolyte solutions were prepared in the flush box using MeCN with 0.5 M $LiClO_4$ as supporting electrolyte. Except for DecaMeFc and MV, which had limited solubility, all of the redox couples were prepared at initial concentrations of ~10 mM. Bulk electrolysis was used to generate the reduced form of MV, as well as all the oxidized forms of the metallocenes except Cc.

Improved buffered HF (BHF, Transene) was used to etch any native oxide on the p-Si wafer pieces immediately before coating with graphene or hexagonal boron nitride. BHF was also used to clean bare p-Si electrodes immediately before electrochemical testing of the bulk properties.

CVD-grown monolayer graphene on Cu (Cu/Gr) was purchased from Advanced Chemical Supplier Materials (Medford, MA). Grains of graphene from this source are known to be around 50 μm in diameter as reported by the manufacturer. Monolayer hexagonal boron nitride grown by chemical vapor deposition on copper (Cu/h-BN) was purchased from Graphene Supermarket. Grains of h-BN from this source are known to be approximately 5 μm in diameter as reported by the manufacturer.

For electrochemical measurements, double-side polished, boron-doped, p-type Si(111) wafers (0.3 Ω cm resistivity, $N_A = 7 \times 10^{16}$ cm^{-3}) were obtained from Addison Engineering, Inc.

Electrode fabrication

Ohmic back contact to the back side for all the p-type silicon wafers used in this study were formed by evaporation of 100nm of gold (Labline Electron Beam Evaporator, Kurt J. Lesker) followed by an anneal at 350°C under forming gas (H_2(g):N_2(g) v:v 5:95). Wafer pieces used in SECCM studies were also lithographically patterned with registry marks to track the location of the electrochemical measurements and ensure that data were collected on intact portions of the 2D material monolayer.

Since the hexagonal boron nitride used in this study was grown on copper as the graphene was, electrodes for both were made analogously. The methods for the graphene electrodes are detailed here. To make the coated electrodes, a strip of copper covered by monolayer graphene (Cu/Gr) was coated with a supporting polymer layer of 495K A4 polymethyl methacrylate (PMMA, MicroChem) at 3000 rpm for 60 s. The resulting stack (Cu/Gr/PMMA) was then cured for 5 minutes at 120°C. Smaller pieces matching the desired size of the fabricated electrodes were cut and etched in a $FeCl_3$ etch solution (Copper etch, Transene) until the copper was gone by visual inspection, approximately 1.5h. This copper-free piece (Gr/PMMA) was transferred to a ≥18MΩ-cm resistivity water bath for 1h before transfer to a second clean water bath were it was left for 12h. After transfer to a final fresh water bath, the stack was pulled onto a p-Si wafer piece that had been etched with improved buffered HF (Transene), dried thoroughly using a gentle stream of nitrogen, and heated to 80°C for 10 minutes to allow the PMMA layer to reflow. The substrate was then rinsed in acetone for 10 minutes before being annealed for 2h at 350°C in a reducing atmosphere (H_2(g):Ar(g) v:v 5:95) to remove any residual PMMA from the transfer process.

The p-Si/Gr stack was attached to a Cu wire using Ga-In eutectic alloy and high purity silver paint (SPI Supplies, West Chester, Pennsylvania). The back of the electrode was covered with a layer of clear nail polish to prevent any leakage of the Ga-In eutectic. Then the sample was sealed to a Pyrex tube with a layer of Loctite 9460 Hysol epoxy and allowed to cure overnight. The area of the resulting electrode was measured using ImageJ to analyze optical images of each electrode.

For the macroscale measurements, a set of control electrodes (p-SiOx) were made analogously to the p-Si/Gr and p-Si/h-BN electrodes described above. In brief, a layer of PMMA was spun onto bare copper foil to generate a PMMA/Cu stack. This stack was processed identically to the PMMA/Gr/Cu stacks to yield p-Si-H with no 2D overlayer. The samples will be referred to as p-SiO_x or blank electrodes as the processing and annealing steps generated a small amount of silicon oxide on the surface, in contrast with the p-Si-H electrodes, which were etched with improved buffered HF immediately prior to testing to completely remove any oxide.

SECCM samples were made analogously to the bulk process above with the Gr and h-BN samples transferred to the same p-Si wafer chip to ensure uniformity between the two materials. After annealing, the sample was attached through the back contact to a custom SECCM stage for analysis.

Hall samples were prepared by transferring graphene using the methods detailed above to p-Si with a 300 nm thermal oxide. Gold top contacts were deposited by e-beam evaporation with a thin titanium adhesion layer.

Electrochemical Methods

Bulk electrolysis was performed in a four-neck round bottom flask inside a N_2 flush box with <3 ppm O_2. The working and counter electrodes were Pt meshes, while the reference electrode was a Pt-polypyrrole reference electrode prepared in a 0.5 M $LiClO_4$-MeCN solution. The reference and counter electrodes were each contained in separate compartments constructed from borosilicate tubing with a Vycor porous glass frit attached to the end with Teflon heat-shrink tubing. Each compartment was filled with 0.5 M $LiClO_4$-MeCN solution. Progress of the bulk electrolysis was monitored by cyclic voltammetry using a 12.5 μm radius Au ultramicroelectrode.

All macroscale measurements were performed inside an Ar drybox with <0.5 ppm O_2 using a SP-200 Biologic potentiostat. The reference electrode was a platinum wire coated with a layer of polypyrrole (Pt-PPy), deposited from a 10 mM solution of pyrrole in 0.5 M $LiClO_4$-MeCN following established procedures.[1] The reference was remade for testing with each redox couple and consistently produced a stable potential around +0.2 V vs. Ag/AgCl. Cyclic voltammograms on p-Si–H, pSiOx, p-Si/Gr, and p-Si/h-BN using each redox couple were recorded at 50 mV/s scan rate under illumination and in the dark. Open circuit potential was measured multiple times for each electrode, although the duration of the measurements were adjusted for different redox couples and locations to allow enough time for V_{OC} to stabilize.

Pipettes for SECCM were prepared using a Sutter Instruments P-2000 laser puller. Quartz theta capillaries (1.2 mm O.D., 0.9 mm I.D, Sutter Instruments) were first cleaned with acetone and methanol, then pulled to create pipettes with openings from 50-500 nm radius. The pipettes were then silanized with chlorotrimethylsilane to create a hydrophobic surface. Pipettes were filled with electrolyte solutions using a glass syringe and a stainless steel needle.

All SECCM measurements were performed using a CHI 920D inside a N_2 flush box with < 3 ppm O_2. The counter and reference electrodes were 0.2 mm Pt wires, each on opposite sides of the theta pipette, and the p-Si photoelectrode was the working electrode. Prior to approaching the surface, pipettes were positioned within 20 microns of the surface using an endoscope. The substrate was then biased positive with respect to the reference electrode as pipettes were brought towards the surface. Movement automatically stopped when the potentiostat detected the current spike that occurred when a liquid junction formed. Illumination for photoelectrochemical SECCM experiments was provided at a 45° angle by fiber optic attached to an ELH lamp inside the flush box that gave a measured illumination intensity equivalent to 1 sun. As in the macroscale measurements, cyclic voltammograms at each location using each redox couple were recorded at 50 mV/s scan rate under illumination and in the dark. Open circuit potential measurement times were adjusted for different redox couples and locations to allow enough time for V_{OC} to stabilize.

Instruments

X-ray photoelectron spectroscopic (XPS) data were collected at 1E-9 Torr using a Kratos AXIS Ultra DLD with a magnetic immersion lens that consisted of a spherical mirror and concentric hemispherical analyzers with a delay-line detector (DLD). An Al Kα (1.486 KeV) monochromatic source was used for X-ray excitation. Ejected electrons were collected at a 90° angle from the horizontal. The CASA XPS software package v 2.3.16 was used to analyze the collected data.

Carrier mobilities were obtained using an H-50 MMR Hall Measurement System. Raman spectra were collected with a Renishaw Raman microscope at λ=532 nm through an objective with numerical aperture=0.75. The laser power was ~3 mW. UV/Vis transmission spectra were collected with a Cary 5000 absorption spectrometer equipped with an external DRA 1800 attachment. The data were automatically zero/baseline corrected by the instrument before any additional processing was performed.

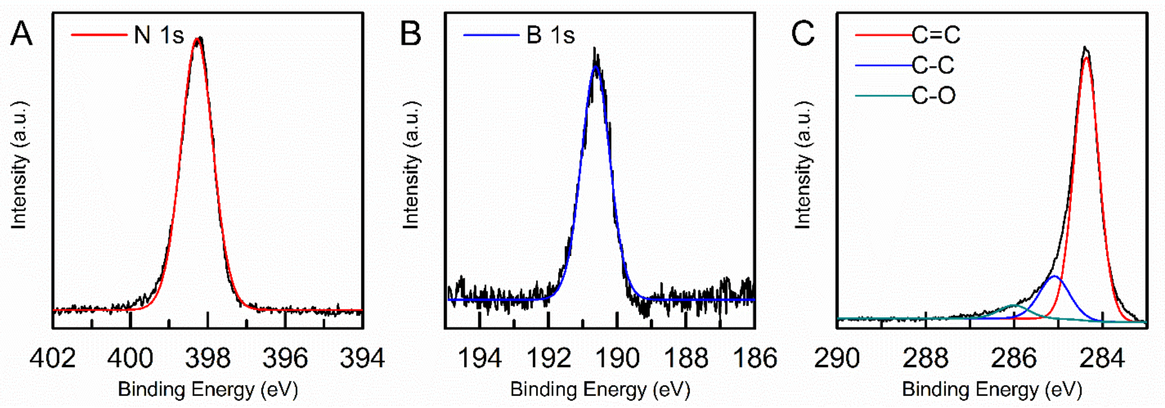

Figure 1. X-ray photoelectron spectra of A) the N 1s and B) the B 1s region of a typical p-Si/h-BN sample and C) the C 1s region of a typical p-Si/Gr sample.

Results

Characterization

The graphene and hexagonal boron nitride used in this study were fully characterized using x-ray photoelectron spectroscopy, Raman spectroscopy, and UV/vis spectroscopy. In addition, measurements of the Hall mobility of graphene were collected for four different devices, yielding an average value of 968 $cm^2/V*s$ as expected for monolayer polycrystalline graphene.

Figure 1 shows the X-ray photoelectron spectra for typical p-Si/Gr and p-Si/h-BN samples after anneal under forming gas. Figure Xa-b displays the N 1s and B 1s regions of an h-BN sample with single peaks at 398.3 eV and 190.6 eV respectively, yielding a 1:1 ratio of B:N from the area after adjusting for elemental relative sensitivity factors. The C 1s region of a p-Si/Gr sample in Figure Xc has three peaks at 284.4 eV, 285.0 eV, and 286.1 eV, assigned to the sp^2 carbon bonds of graphene and the residual C-C and C-O bonds of the PMMA transfer support respectively.

Figure 2 shows the x-ray photoelectron spectra of the Si 2p region for a typical p-Si/Gr and p-Si/h-BN samples from this work. The peaks at 99.2 and 99.8 eV are assigned to the Si $2p_{1/2}$ and $2p_{3/2}$ peaks respectively. The peak at 102.5 eV is attributed

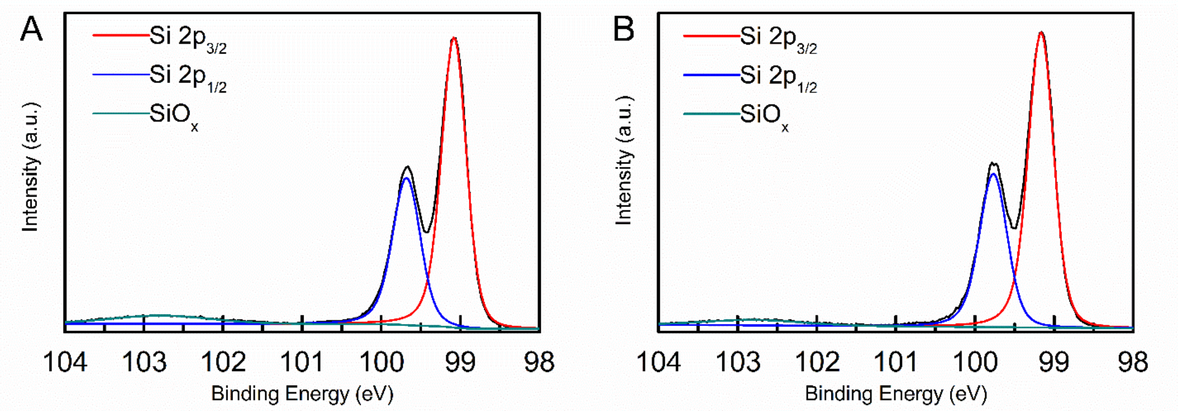

Figure 2. X-ray photoelectron spectra of p-Si surfaces. (A) The Si 2p region of a p-Si/Gr electrode after fabrication. (B) The Si 2p region of a p-Si/h-BN electrode after fabrication. The peaks at 99.2 and 99.8 eV are assigned to the Si $2p_{1/2}$ and $2p_{3/2}$ peaks respectively, while small peak at 102.5 eV is attributed the oxide formed during the fabrication process.

to the formation of oxide on the surface. Indeed, a small amount of oxide is expected from the fabrication process, due to the brief exposure of the surface to water during the transfer process. The thickness of this oxide was quantified using a simple substrate-overlayer model

$$d = \lambda_{ov} \sin\theta \left[\ln\left(1 + \frac{I_{Si}^{o}}{I_{ov}^{o}} * \frac{I_{ov}}{I_{Si}}\right)\right]$$

where λ_{ov} is the attenuation factor through the oxide overlayer (2.6 nm), θ is the angle from the surface to the detector, I_{Si}^{o}/I_{ov}^{o} is the instrument normalization factor expected from uncontaminated Si and SiO_2 samples, which was taken as 1.3 for this instrument, I_{ov} is the measured intensity of the silicon oxide peak found around 103 eV, and I_{Si} is the measured intensity of the silicon. [2,3] Using this equation, an oxide of approximately 0.22 nm was detected on the p-Si/Gr electrodes and an oxide of approximately 0.23 nm was detected on the p-Si/h-BN electrodes. As a monolayer of oxide is about 0.35 nm thick,[3] the average electrode tested in this work had less than a monolayer of oxide growth after the fabrication process.

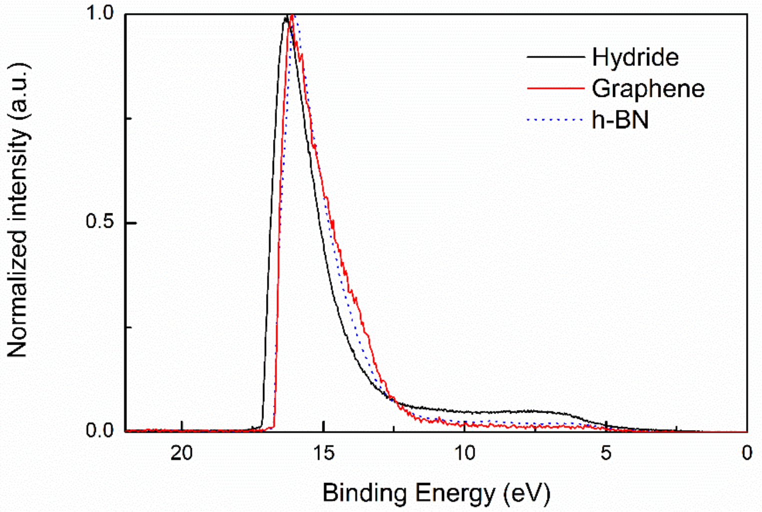

Figure 3. Ultraviolet photoelectron spectra of annealed p-Si-H, p-Si/Gr and p-Si/h-BN samples, corrected with reference to a sputter-cleaned Au sample.

The effect of the fabrication process on each sample was also followed by ultraviolet photoelectron spectroscopy (UPS) to understand the band positions of each type of sample. Figure 3 shows the normalized UP spectra of annealed p-Si-Gr and p-Si/h-BN samples. The secondary electron cutoff (SEC) of both shifted equally from the SEC of the annealed p-Si-H sample. The work function (W_F) of each sample was calculated by extrapolating the slope of the SEC to its intercept with the x-axis and subtracting that value from the excitation energy of He I (21.21 eV). The data before and after annealing are shown in Table 1. The magnitude of the work function for p-Si-H is attenuated from the value calculated from the dopant density (N_A=7x10^{16} cm^{-3}, W_F=5.02 eV, $E_{VBM}{}^B$=0.14 eV) but is consistent with the band-bending and dipole expected on this surface.[4] The increase in the work function of p-Si/h-BN is attributed to the formation of oxide during annealing by water trapped at the p-Si/h-BN interface during transfer, attenuating the surface dipole.

Table 1. Secondary electron cutoff, dipole, and work function of samples

	Before anneal				After anneal			
Sample	SEC eV	E_{VBM}^S eV	δ eV	W_F^S eV	SEC eV	E_{VBM}^S eV	δ eV	W_F^S eV
p-Si–H	16.82	0.59	-0.19	4.39	16.93	0.53	-0.36	4.28
p-SiO_x	16.43	0.29	-0.09	4.78	16.50	0.30	-0.16	4.71
p-Si/Gr	16.51	0.41	-0.06	4.70	16.48	0.56	+0.12	4.73
p-Si/ h-BN	16.58	0.53	-0.08	4.63	16.57	0.49	-0.04	4.64

Figure 4 displays the typical Raman spectrum for Gr and h-BN respectively along with contour plots of the surfaces. The Raman spectrum of Gr displays three peaks at 1595 cm^{-1}, 2464 cm^{-1}, and 2691 cm^{-1}, arising from the E_{2g} and A_{1g} modes of the lattice.[5] The primary peaks at 1595 cm^{-1} and 2691 cm^{-1} are known as the G and 2D peaks respectively. The ratio of these peaks (I_G/I_{2D}) is used to understand the integrity of graphene with intact graphene having a ratio of 0.4 to 0.6. In contrast, the Raman spectrum of h-BN has a single peak at 1367 cm^{-1} and so contour plots can only show the relative intensity of different spots on a sheet of h-BN.[6] Each contour plot exceeds the size expected for a single grain of Gr or h-BN, given an average diameter of 50 μm and 5 μm respectively. The scale for each plot is set so that regions with no intensity should be bright blue to differentiate between regions of variable and no intensity. For the graphene contour plot, 95% of values for the ratio of the G to 2D peak are found above 0.4 as expected for monolayer Gr. The dark spots on the plot correspond to a decreased ratio of these two peaks but not to a concomitant increase in the D peak at 1350 cm^{-1}, which would indicate defects in the sheet.[7] As only a single peak is present in a Raman spectrum of h-BN, the contour plot of h-BN displays peak intensity at each point. While intensity varies across the h-BN sheet, there are no voids visible at this scale.

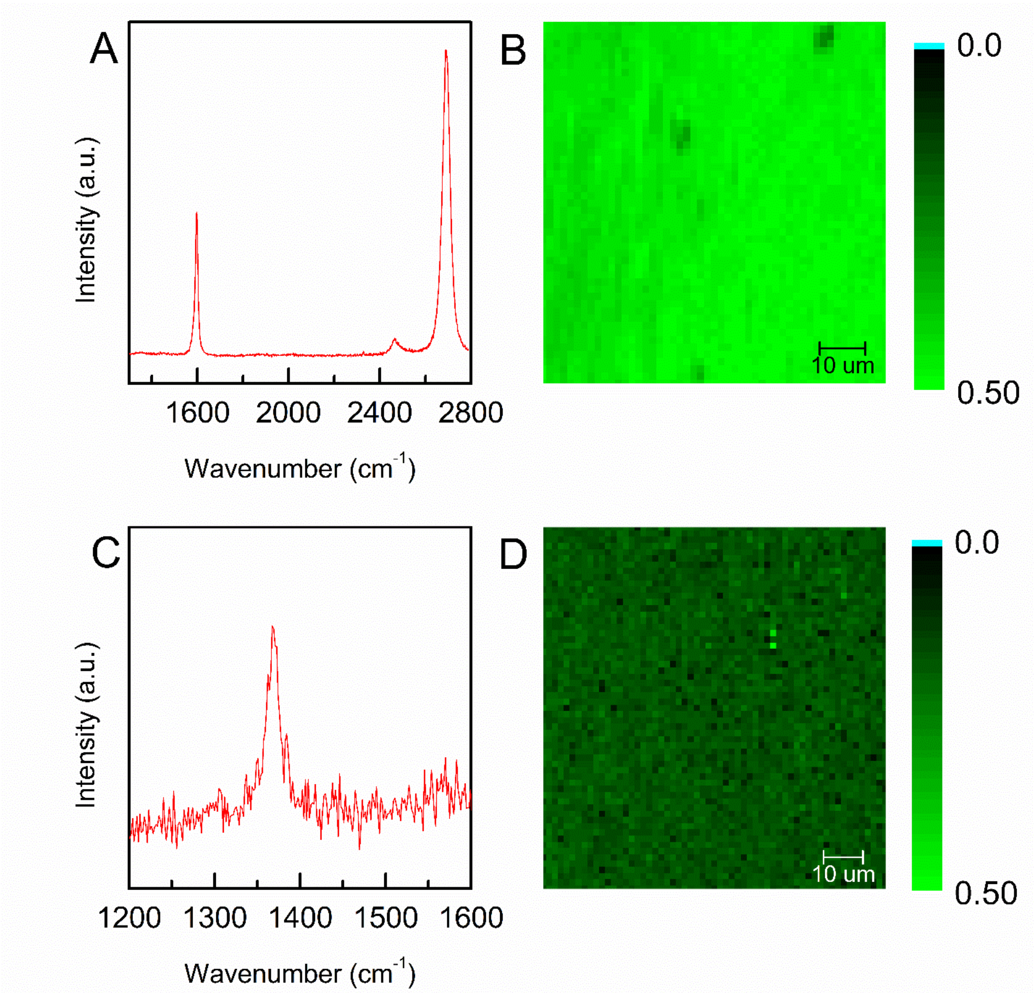

Figure 4. Raman spectra of Gr and h-BN on 300 nm SiO_2. (A) A typical Raman spectrum for a Gr sample with two main peaks at 1595 cm^{-1} (G) and 2691 cm^{-1} (2D). (B) Contour plot of the ratio of the 2D to G peak intensities for a typical monolayer Gr sample from a Raman map. (C) A typical Raman spectrum for an h-BN sample with a single peak at 1367 cm^{-1}. (D) Contour plot of the peak intensity for a typical monolayer h-BN sample from a Raman map. While intensity varies across the sample, the data indicates that the 1370 cm^{-1} peak is present in each spectra. Both contour plots display data for a 75x75 μm region on the sample, which should exceed the size of single grain on either 2D material. For each plot, bright blue is used for an intensity of zero to highlight any voids in the lattice, although none are visible.

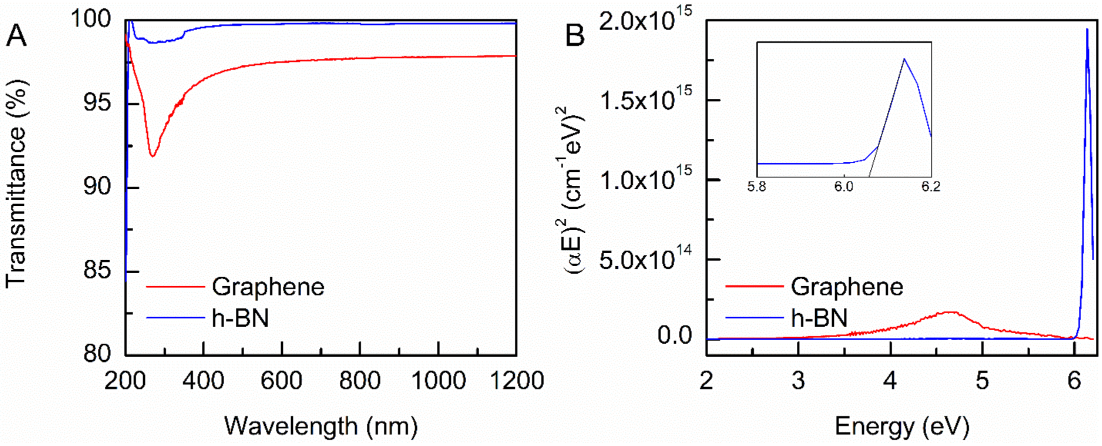

Figure 5. UV/Vis spectra for (A) Gr and h-BN samples on quartz slides and (B) the Tauc plot for h-BN and Gr. The fit for h-BN is shown in the inset.

Figure 5 displays the UV/vis spectra for Gr and h-BN on quartz. h-BN shows almost absorption across the visible light region (400-700 nm), while Gr absorbs 2.7% of light in the same region. The optical bandgap of h-BN was determined to be 6.07 eV from extrapolation of the linear region of the Tauc plot to an intercept with the x-axis, which is within the typical bounds for the polycrystalline material.[8] The same plot for the graphene shows no such sharp increase indicative of the presence of a bandgap.

Electrochemistry

Figure 6 compares the representative macroscale (A-B)and SECCM (C-D) behavior of current with respect to potential for p-Si, p-Si/Gr, and p-Si/h-BN electrodes in the dark and under 100 mW cm^{-2} ELH-s illumination in 0.5 M $LiClO_4$-MeCN solutions containing either Fc or Cc. Additional samples referred to as p-SiO_x, or “blank” electrodes, in reference to the small amount of oxide grown on the surface during fabrication (see Methods for more detail), are also included in the macroscale measurements to show the behavior of the Si wafer when it was subjected to the same processing steps as the p-Si/Gr and p-Si/h-BN electrodes without actually transferring a 2D overlayer to the surface. For macroscale electrodes (Figure 6A, C), the bare p-Si-H and p-SiO_x electrodes exhibited rectifying behavior toward both redox couples, as indicated by cathodic photocurrent under reverse bias. In Fc, p-Si/h-BN electrodes exhibit minimal rectification under illumination, but still have a significant current under reserve bias in the dark. In Cc, these electrodes show strong rectification with only minimal dark current and a large photocurrent. In contrast, the p-Si/Gr samples exhibit ohmic behavior in the Fc solution and moderately rectifying behavior in the Cc solution, as shown by the rapid increase in currents under forward bias for both of these sample types in the dark. Similar behavior for all samples was observed by SECCM (Figure 6B, D). While the macroscale measurements are shown as current density versus potential, the same metric is not used for the SECCM measurements due to effect of pipette tip size on resulting current density. Thus, the SECCM data is graphed as a ratio of the current to the steady-state current (i/i_{ss}), a ratio commonly used in the SECCM literature.

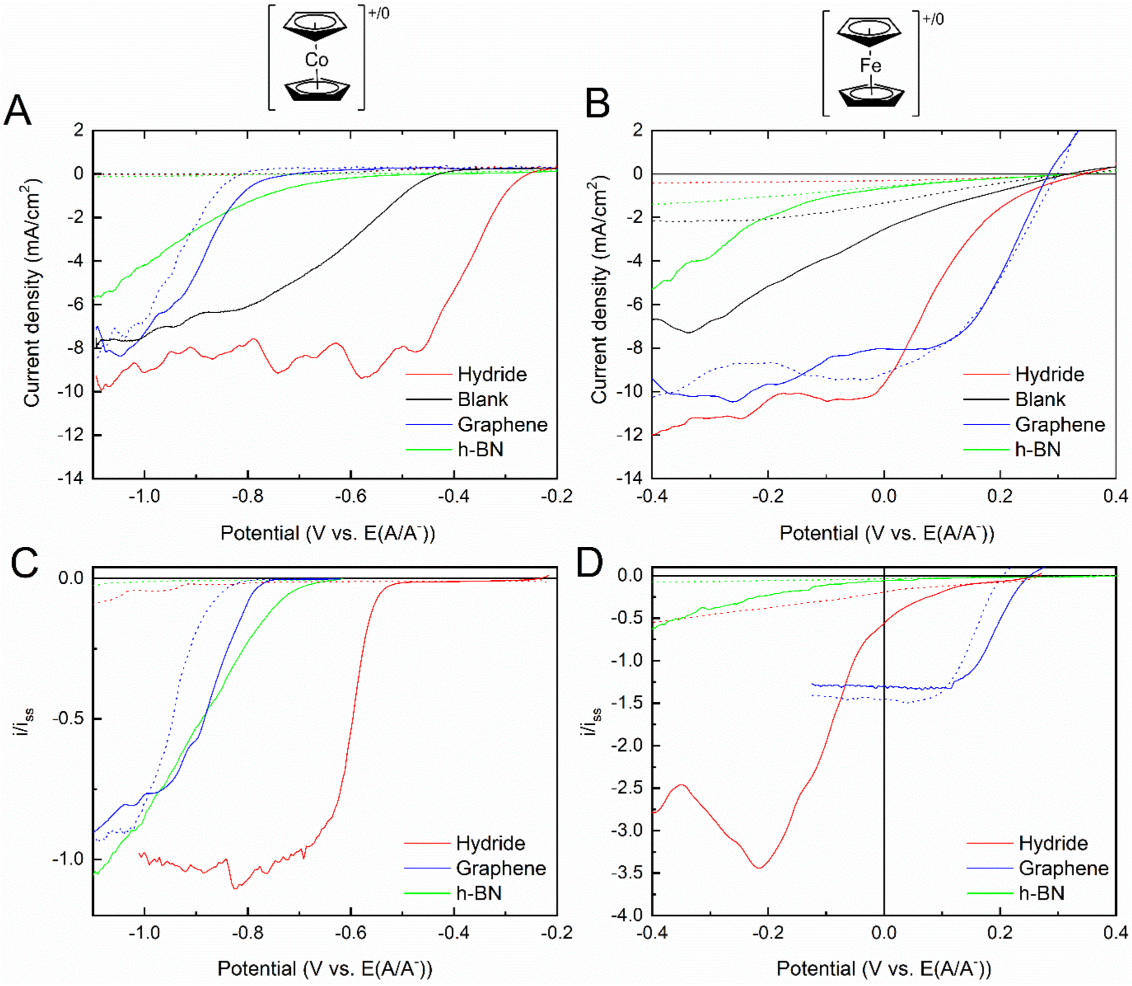

Figure 6. Photocurrent density-potential (J-V) performance of p-Si electrodes in contact with cobaltocene (A, C) and ferrocene (B, D) in CH_3CN–0.5 M $LiClO_4$ under 100 mW cm^{-2} ELH illumination. The dashed lines show scans of the same electrodes without illumination. In both sets of data, the fill factor of p-Si/h-BN electrode is significantly worse than either the p-Si-H or p-SiO_x, while the p-Si/Gr electrode display little to no shift upon illumination as expected in Cc and Fc for a weakly rectifying or ohmic contact respectively with solution.

Figure 7 shows the dependence of V_{OC} on the effective solution potential for p-Si–H, p-Si/Gr, and p-Si/h-BN in contact with 1.0 M $LiClO_4$−CH_3CN under 100 mW cm^{-2} ELH-type illumination. Each point represents an average of at least 5 electrodes with standard deviations represented by the error bars. Since the effective potential of Fc and DiMeFc were very close, only data for Fc is shown in Figure 7 for clarity. The V_{OC} data for DiMeFc can be found in Table 2. In both the macroscale and SECCM measurements, the p-Si–H, $pSiO_x$, and p-Si/h-BN samples show two distinct trends: regions at relatively positive or negative $E_{eff}(A/A^-)$ where V_{OC} is fixed with respect to $E_{eff}(A/A^-)$ and a second region where V_{OC} scales approximately linearly with V_{OC}. The slopes of V_{OC} with respect to effective potential is lower than reported previously, but the maximum ΔV_{OC} of 470±57 mV for p-Si–H is comparable with the previously reported value of 523±42 mV.[9] The p-Si–H samples in this work display a slope around 0.50 while the $p\text{-}SiO_x$ and p-Si/h-BN samples both have a slope around 0.35. The p-Si/Gr samples display the least change in V_{OC} across the full range of redox couples, shifting only in couples with sufficiently negative $E_{eff}(A/A^-)$ with a slope around 0.10. This is true for both the macroscale and SECCM measurements. The maximum ΔV_{OC} for p-Si–H by SECCM is 342±18 mV, which is closer to 401±33 mV, the maximum ΔV_{OC} value for the macroscale $p\text{-}SiO_x$ measurements. As the p-Si—H, p-Si/Gr, and p-Si/h-BN measurements were all taken on the same wafer chip to ensure uniformity in sample preparation, it was not possible to etch the p-Si–H surface immediately before testing, leaving a small amount of oxide on the surface, similar to the preparation of the $p\text{-}SiO_x$ electrodes described previously. Experimental conditions and all V_{OC} data for the macroscale and SECCM measurements are summarized in Table 2.

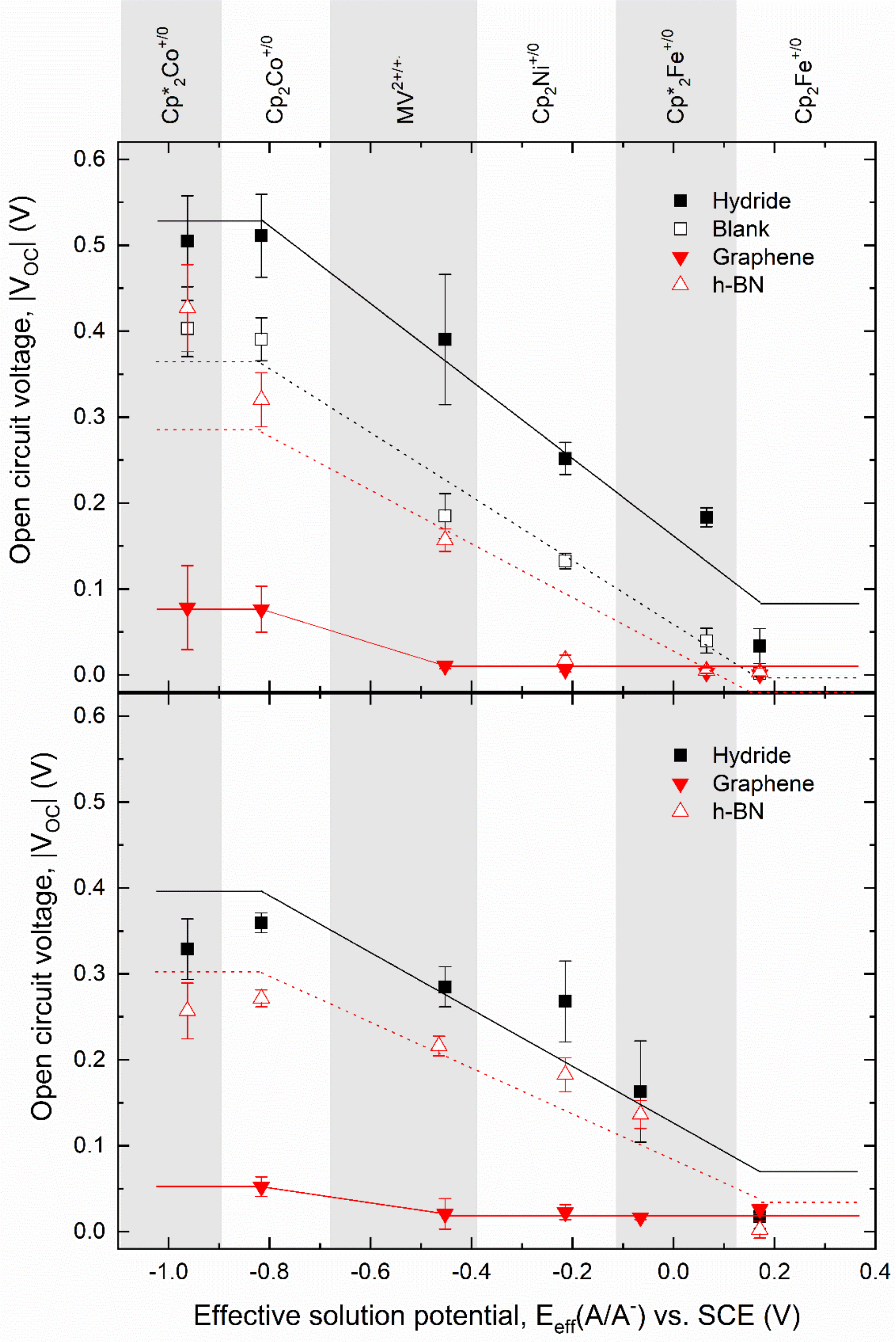

Figure 7. Comparison of open-circuit potential of p-Si–H, p-SiO$_x$, p-Si/Gr, and p-Si/h-BN electrodes versus the effective potential of various redox couples for macroscale electrodes (upper) and by SECCM (lower). Three regions have been identified for all samples. These regions are highlighted with lines meant to guide the eye.

Table 2. Summary of experimental conditions and results [a]

	concentration (mM)		effective potential vs. SCE (V)	V_{OC} (V) from macroscale electrodes				V_{OC} (V) from SECCM electrode		
	ox	red		p-Si–H	p-SiO_x	p-Si/ Gr	p-Si/ h-BN	p-Si–H	p-Si/ Gr	p-Si/ h-BN
decamethylcobaltocene$^{+/0}$ $Cp^*{}_2Co^{+/0}$	5.7	0.4	-0.963	0.505(53)	0.403(33)	0.078(49)	0.427(50)	0.329(35)	-[b]	0.257(32)
cobaltocene$^{+/0}$ $Cp_2Co^{+/0}$	16.6	0.4	-0.816	0.511(48)	0.391(25)	0.077(27)	0.320(31)	0.360(11)	0.052(11)	0.272(10)
methyl viologen$^{2+/+\bullet}$ $MV^{2+/+\bullet}$	2.0	0.1	-0.453	0.390(76)	0.185(26)	0.011(3)	0.157(13)	0.285(23)	0.021(18)	0.216(11)
nickelocene$^{+/0}$ $Cp_2Ni^{+/0}$	0.5	2	-0.214	0.252(19)	0.133(9)	0.006(3)	0.018(6)	0.268(47)	0.023(9)	0.183(20)
decamethylferrocene$^{+/0}$ $Cp^*{}_2Fe^{+/0}$	1.3	0.2	0.065	0.183(11)	0.040(14)	0.003(1)	0.005(3)	0.163(60)	0.017(3)	0.136(16)
dimethylferrocene$^{+/0}$ $Me_2Cp_2Fe^{+/0}$	10.6	2.4	0.167	0.087(48)	0.005(3)	0	0	0.066(12)	0.018(5)	0.019(9)
ferrocene$^{+/0}$ $Cp_2Fe^{+/0}$, or $Fc^{+/0}$	12.9	0.7	0.171	0.034(20)	0.002(1)	0	0.003(5)	0.018(14)	0.026(5)	0.002(10)

[a] Each value of V_{OC} represents measurements from at least six photoelectrodes on the macroscale and at least three spots by SECCM. Standard deviations are given in parentheses, where appropriate.

[b] Due to the lack of stability in the decamethylcobaltocene couple, no SECCM measurements could be collected for the p-Si/Gr interface

Figure 8 shows line scans of V_{OC} by SECCM for p-Si/Gr and p-Si/h-BN in contact with Cc, Nc, and DiMeFc. These measurements were taken in consecutive 10 μm steps, although each scan with a different redox couple was collected on a separate region of the sample in order to avoid cross contamination of the redox species. For p-Si/Gr, the measurements for Nc and DiMeFc are very similar and show little spatial variation across the measured region. The V_{OC} values for pSi/Gr in contact with Cc are distinctly higher but also show relatively little spatial variation. The V_{OC} of p-Si/h-BN sample in contact with the same redox couples shifts over a much wider range of potentials. For both samples, the V_{OC} does not vary significantly across the surface, despite the presence of grain boundaries in the polycrystalline material. The measurements of V_{OC} in contact with Nc shows the largest variation across the surface on both the p-Si/Gr and p-Si/h-BN.

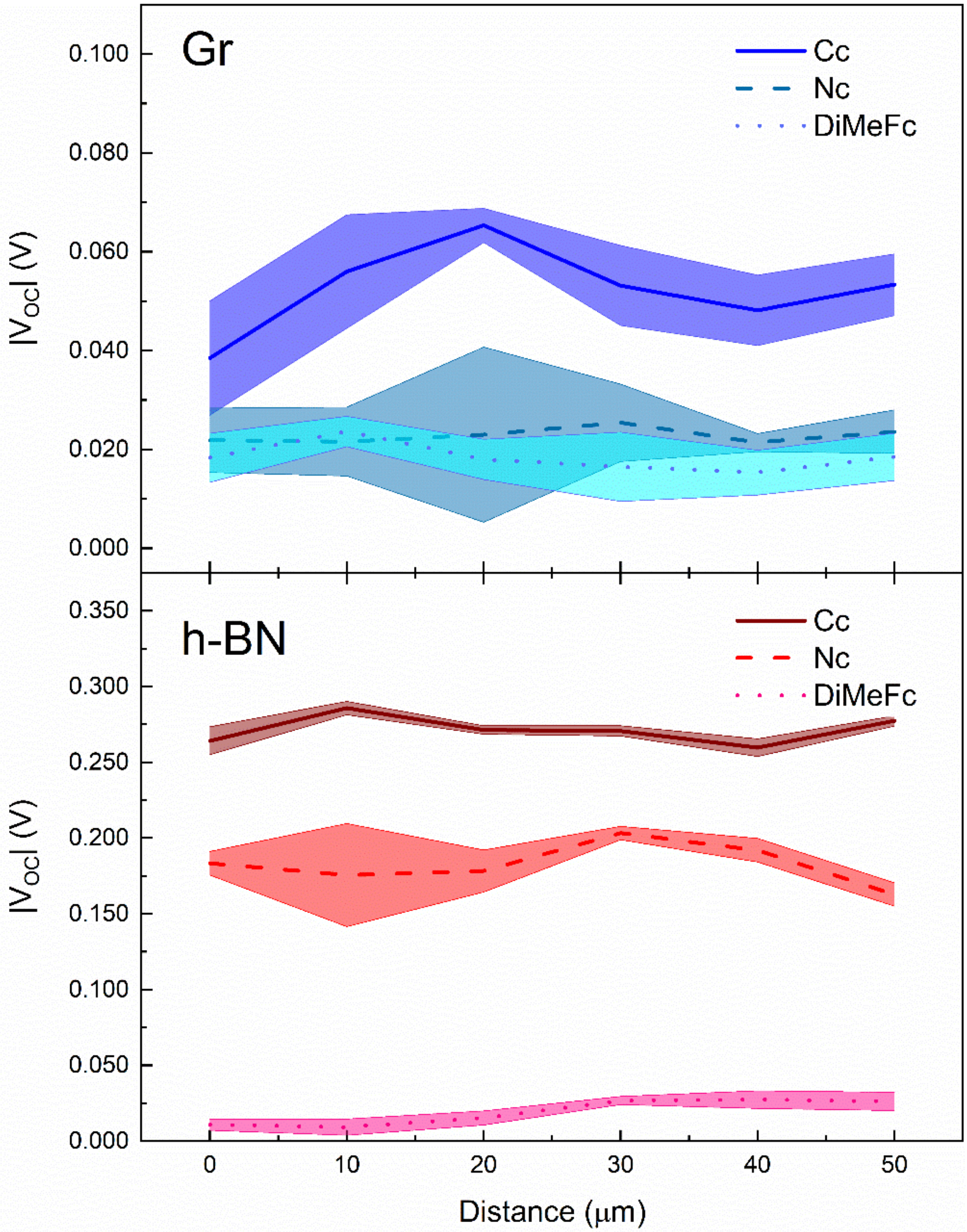

Figure 8. SECCM line scan of V_{OC} in 10 μm steps on Gr (upper) and h-BN (lower) in contact with Cc, Nc, and DiMeFc. Each value is the average of six measurements at the same spot. Standard deviations are represented by the shaded regions surrounding each scan.

Discussion

During macroscale testing, six replicate photoelectrodes were tested for each redox couple. Each photoelectrode was used to measure V_{OC} against a single redox couple to avoid testing samples that may have degraded through use. Specifically, this procedure guards against using samples where graphene has delaminated from the Si surface due to capillary forces produced as the electrolyte solvent dries while cleaning and moving a single sample between different solutions. Because of this precaution, the V_{OC} has not been tested against the full range of redox couples for any single electrode. Due to the small spot size of SECCM, the full complement of redox couples could be measured on a single 1 cm^2 sample containing bare regions and regions covered separately by Gr and h-BN, thereby allowing their distinct behaviors to be elucidated.

As shown in Figure 6, measurements of V_{OC} by SECCM generally show excellent agreement with their macroscale counterparts with few exceptions. The values for V_{OC} of p-Si–H at the macroscale are consistently higher than those observed by SECCM. The values of V_{OC} for p-Si–H by SECCM are much closer to the values of V_{OC} for the macroscale p-SiO_x electrodes. This similarity follows from the data in Figure 4, which shows that the same thickness of oxide was generated at the surface of the p-SiO_x electrodes as the p-Si/Gr and p-Si/h-BN electrodes during fabrication. Thus, the bare region of the single electrode used for SECCM is more similar to the silicon surface under Gr or h-BN than to a freshly etched p-Si–H electrode. The oxide then accounts for a decrease in observed V_{OC} of approximately 100 mV.

Additionally, select measurements, such as the V_{OC} of p-Si/h-BN in contact with $Nc^{0/+}$, were lower in the macroscale measurements than in the SECCM. However, these differences are predominantly observed for the less stable redox couples (i.e. DecaMeCc, Nc). The slope in V_{OC} for p-Si–H, p-SiO_x and p-Si/h-BN are identical within error for the macroscale and SECCM measurements, demonstrating the observed trends remain the same across the macro and nanoscale, despite minor discrepancies. Hence, measurements against redox couples spanning a large range of potentials are necessary to fully understand the trend in V_{OC} on a photoelectrode using these techniques.

A comparison of the cyclic voltammetry (Figure 7) shows identical shapes between macroscale and SECCM measurements for these samples, but reveals different behavior between the types of sample. The p-Si–H is strongly rectifying in contact with cobaltocene and has a high value of V_{OC} upon illumination. While the p-Si/h-BN is also rectifying, the shape of the curve under illumination shows much more resistive behavior than that of the p-Si–H. In fact, the light limiting current was not reached until the potential was pushed further negative of the window shown. The p-Si/Gr interface was shown to be weakly rectifying to cobaltocene and shows very little difference in behavior in the dark or under illumination, indicating that it forms a poor interface for charge separation as fabricated. In contact with Fc, all samples are ohmic and display similar shapes to the voltammetry against Cc.

The differences in the values for V_{OC} in the p-Si/Gr and p-Si/h-BN samples could be attributed to the presence of oxide at the surface, increased surface recombination due to the surface oxide or defects in the 2D material overlayer, and the relative density of states of each overlayer. The effect of the oxide on V_{OC} has already been discussed and ΔV_{OC} was calculated to be about 100 mV as compared to the V_{OC} from the pristine p-Si-H surface. However, this does not account for the additional 200-300 mV difference observed between the p-SiO_x and p-Si/2D overlayer electrodes. The similarity in slopes for the p-SiO_x and p-Si/h-BN electrodes suggests that alterations to the expected V_{OC}, the value for p-Si–H at the same potential, can be treated as linear decreases in the overall performance of the p-Si/h-BN electrodes. The difference between the p-Si/h-BN and p-SiO_x samples was consistently 65 mV for both the macroscale and SECCM measurements. In contrast, the p-Si/Gr electrodes have very different behavior over the same range of effective potentials, suggesting that a different mechanism is at work to explain the drastic decrease in V_{OC} observed for these samples.

The samples fabricated in this work used polycrystalline, CVD-grown sheets of monolayer 2D material, which is known to contribute to defects on the surface of a 2D material and provide sites for increased surface recombination.[10,11] A comparison of the surface recombination velocity (SRV) of these samples shows that p-SiO_x samples have a slightly lower SRV (3025 cm s^{-1}) than the p-Si/Gr (4064 cm s^{-1}) and p-Si/h-BN samples (3905 cm s^{-1}) by a factor of 0.33. The difference between the SRV for p-SiO_x and p-Si/2D overlayer could be attributed to the additional recombination sites provided by the defects in the polycrystalline 2D material overlayer; however, while the polycrystallinity of the Gr and h-BN used in this work would contribute to the smaller range of tunable V_{OC} when compared to p-Si–H or p-SiO_x, it would not account for the differences between the p-Si/Gr and p-Si/h-BN samples. In particular, the grains of the h-BN used in this work, and thus the number of atoms involved in bonding at a grain boundary, were smaller than those in the Gr by an order of magnitude. If the crystallinity were the sole factor in limiting the range of potentials at the interface, p-Si/h-BN would be predicted to have lower values of V_{OC} than p-Si/Gr. Since the reverse behavior is observed, the difference in the samples cannot be attributed to the different grain sizes.

As the surface oxide, increase in recombination, and polycrystalline nature of the 2D overlayer only partially account for the difference between p-Si–H and p-Si/Gr or p-Si/h-BN, the properties of the 2D material and interaction with the surface must also contribute significantly to the observed differences. The crystal structure and lattice constants for Gr and h-BN are nearly identical and differ most prominently in the size of bandgap. With a limited density of states near its Fermi level, which is positioned mid-gap to silicon, graphene is more likely to be pinned at the interface than h-BN, which has no states mid-gap or near the conduction or valence band of silicon. This difference between Gr and h-BN is reflected in the values for δ calculated from the XPS data. Both p-Si–H and p-Si/h-BN electrodes after anneal have negative surface dipoles, which contribute beneficially to V_{OC}, although p-Si/h-BN has a significantly smaller surface dipole than p-Si–H. In contrast, the p-Si/Gr electrodes have a positive surface dipole, which lowers the resulting V_{OC}. The original dipole of the p-Si/Gr surface suggests that before the annealing step the p-Si/Gr should have a V_{OC} closer to the values seen on the annealed p-Si/h-BN surface. Similarly, the unannealed p-Si/h-BN samples should have values of V_{OC} close to a freshly etched p-Si–H. Thus, the changes to the surface because of annealing, including removal of polymer residue and growth of the interfacial oxide, affect both p-Si/h-BN and p-Si/Gr interfaces, but are more detrimental to the p-Si/Gr interface due to the reversal of the surface dipole.

Conclusion

This work demonstrates that the macroscale behavior of photoelectrodes can be reliably reproduced on the nanoscale by SECCM. Additionally, the V_{OC} values for p-Si/h-BN and p-Si/Gr demonstrate that the performance of these interfaces is dependent primarily on the position of the Fermi level and density of states relative to band edges of the chosen semiconductor as well as fabrication techniques.

References

1. Ghilane, J., Hapiot, P. & Bard, A. J. Metal/Polypyrrole Quasi-Reference Electrode for Voltammetry in Nonaqueous and Aqueous Solutions. *Anal. Chem.* **78**, 6868–6872 (2006).
2. *Auger and X-ray photoelectron spectroscopy*. (Wiley, 1996).
3. Haber, J. A. & Lewis, N. S. Infrared and X-ray Photoelectron Spectroscopic Studies of the Reactions of Hydrogen-Terminated Crystalline Si(111) and Si(100) Surfaces

with Br2, I2, and Ferrocenium in Alcohol Solvents. *J. Phys. Chem. B* **106**, 3639–3656 (2002).

4. Gleason-Rohrer, D. C., Brunschwig, B. S. & Lewis, N. S. Measurement of the Band Bending and Surface Dipole at Chemically Functionalized Si(111)/Vacuum Interfaces. *J. Phys. Chem. C* **117**, 18031–18042 (2013).
5. Ferrari, A. C. *et al.* Raman Spectrum of Graphene and Graphene Layers. *Phys. Rev. Lett.* **97**, 187401 (2006).
6. Gorbachev, R. V. *et al.* Hunting for Monolayer Boron Nitride: Optical and Raman Signatures. *Small* **7**, 465–468 (2011).
7. Ferrari, A. C. Raman spectroscopy of graphene and graphite: Disorder, electron–phonon coupling, doping and nonadiabatic effects. *Solid State Commun.* **143**, 47–57 (2007).
8. Cassabois, G., Valvin, P. & Gil, B. Hexagonal boron nitride is an indirect bandgap semiconductor. *Nat. Photonics* **10**, 262–266 (2016).
9. Grimm, R. L. *et al.* Comparison of the Photoelectrochemical Behavior of H-Terminated and Methyl-Terminated Si(111) Surfaces in Contact with a Series of One-Electron, Outer-Sphere Redox Couples in CH3CN. *J. Phys. Chem. C* **116**, 23569–23576 (2012).
10. Denis, P. A. & Iribarne, F. Comparative Study of Defect Reactivity in Graphene. *J. Phys. Chem. C* **117**, 19048–19055 (2013).
11. Banhart, F., Kotakoski, J. & Krasheninnikov, A. V. Structural Defects in Graphene. *ACS Nano* **5**, 26–41 (2011).